Stress-induced anisotropic diffusion in alloys: Complex Si solute flow near a dislocation core in Ni

Thomas Garnier,[1,2] Venkateswara R. Manga,[1,3] Dallas R. Trinkle,[1,*] Maylise Nastar,[2] and Pascal Bellon[1]
[1]*Department of Materials Science and Engineering, University of Illinois, Urbana-Champaign, Illinois 61801, USA*
[2]*CEA, DEN, Service de Recherches de Métallurgie Physique, 91 191, Gif-sur-Yvette, France*
[3]*University of Arizona, Materials Science and Engineering, Tucson, Arizona 85721, USA*
(Received 22 February 2013; revised manuscript received 13 July 2013; published 25 October 2013)

Stress introduces anisotropy in the transport coefficients in materials, affecting diffusion. Using first-principles quantum-mechanical methods for activation barriers of atomic jumps, combined with the extended self-consistent mean-field theory to compute transport coefficients with strain-reduced symmetry, we predict significant stress-induced anisotropy for Si impurity diffusion in nickel. This causes complex spatial- and temperature-dependent fluxes; as an example, the heterogenous strain field of a dislocation creates unusual flow patterns that affect mechanical and segregation behavior.

DOI: 10.1103/PhysRevB.88.134108 PACS number(s): 66.30.−h, 61.72.J−, 61.72.Lk

I. INTRODUCTION

Stress effects on atomic diffusion are ubiquitous, often modifying the evolution of microstructures and properties of materials. Externally applied stresses delay the coarsening kinetics of precipitates in superalloys;[1] epitaxial stresses in semiconductor thin films cause anisotropic dopant diffusion, impacting device characteristics;[2–4] internal stress fields near a dislocation modify transport and segregation of C solute atoms in Fe,[5,6] and control creep in pure metals;[7,8] and stresses produce anisotropy in electromigration,[9] and surface diffusion.[10] Stress affects the driving force for diffusion—the gradient of chemical potentials—as well as transport coefficients—the so-called Onsager, or phenomenological coefficients. Previous work on stress effects on diffusion has mainly focused on the former effect,[11] although the latter can significantly affect transport kinetics. Nonhydrostatic stress can lower the crystal symmetry, leading to anisotropic diffusion even in materials that are cubic without stress. Atomic simulations reveal that anisotropy can change sign with the crystal orientation: In face-centered cubic (FCC) Cu and Pt under compressive biaxial stress, dumbbell interstitial atoms diffuse faster out-of-plane than in-plane for a (111) plane, but surprisingly the opposite is true for a (100) plane.[12] One determining factor of anisotropy is the symmetry of the saddle-point configurations for the point defects responsible for atomic transport.[7,13]

Despite these important results, little attention has been paid to stress-induced anisotropic transport in alloys with coupled point-defect and solute diffusion. With recent advances of atomistic techniques, defect and atom jump frequencies are calculable from first principles.[14,15] The main challenge remains determining *macroscopic transport coefficients* generated by stress-modified jump frequencies. We overcome this difficulty by extending the self-consistent mean-field theory.[16–18] We demonstrate the potential of this combined approach by considering the effect of stress on vacancy-mediated transport of Si atoms, and solute flux near a dislocation core in Ni. This approach predicts remarkable solute flow patterns around dislocation cores, with complex temperature dependence from the anisotropic kinetic coupling between vacancies and Si atoms.

In a multicomponent system, like Si in Ni, fluxes and chemical potential gradients are related by the transport coefficients. For vacancy-mediated diffusion, there are three independent transport coefficients L_{SiSi}, L_{VV}, and L_{SiV},

$$\begin{aligned} j_{\mathrm{Si}} &= -L_{\mathrm{SiSi}}\nabla\mu_{\mathrm{Si}} - L_{\mathrm{SiV}}\nabla\mu_{\mathrm{V}}, \\ j_{\mathrm{V}} &= -L_{\mathrm{VV}}\nabla\mu_{\mathrm{V}} - L_{\mathrm{SiV}}\nabla\mu_{\mathrm{Si}}. \end{aligned} \tag{1}$$

Each L_{AB} is a second-rank tensor; cubic symmetry results in isotropy (equal diagonal components, zero off-diagonal components). The chemical potential for vacancies and solutes has the usual form, with the addition of (small) volumetric strain ε_{v} times a proportionality constant α

$$\begin{aligned} \mu_{\mathrm{V}} &= \alpha_{\mathrm{V}}\varepsilon_{\mathrm{v}} + k_{\mathrm{B}}T\ln\left(\gamma_{\mathrm{V}}c_{\mathrm{V}}/c_{\mathrm{V}}^{0}\right) \\ \mu_{\mathrm{Si}} &= \alpha_{\mathrm{Si}}\varepsilon_{\mathrm{v}} + k_{\mathrm{B}}T\ln\left(\gamma_{\mathrm{Si}}c_{\mathrm{Si}}/c_{\mathrm{Si}}^{0}\right), \end{aligned} \tag{2}$$

where c_{V}^{0} and c_{Si}^{0} are equilibrium concentrations without strain or other defects, and γ_{V} and γ_{Si} are activity coefficients. The attractive Si-vacancy binding energy (–0.1 eV for first neighbor) forms Si-vacancy complexes and so L_{SiV} can be positive at low temperature as vacancies drag solute along with their flow, but becomes negative at higher temperatures as entropy destabilizes these complexes.

Even for "simple" cases, such as vacancy-mediated solute diffusion in an FCC crystal with five distinct jump frequencies,[19,20] the derivation of L_{AB} is not straightforward. Closed-form solutions that include the effect of correlated jumps are not straightforward due to kinetic correlations. For example, if a solute exchanges back-and-forth with a vacancy, there is no diffusion. When symmetry is broken by strain, the number of distinct atomic jump types increases. The self-consistent mean-field (SCMF) kinetic theory relates atomic-scale mechanisms for diffusion to macroscopic transport coefficients.[16–18] SCMF kinetic theory finds a steady-state solution to the master equation—based on atomic jumps rates between states—in the presence of a small chemical potential gradient. The equilibrium solution for state occupancy probability is proportional to a Boltzmann factor for a lattice Hamiltonian with interacting solute and vacancies; the steady-state solution includes an additional effective Hamiltonian to capture kinetic correlations, and is dependent on the driving force type. In the dilute limit, there are only pair interactions and the mean-field solution is exact. The chemical potential gradient produces a "bare" flux combined with a

TABLE I. Activation energies (eV) for different jumps of a vacancy in stress-free Ni with a Si atom. The Si-vacancy binding energies are −0.100 eV, 0.011 eV, and 0.045 eV for first ($\frac{1}{2}\langle 110\rangle$), second ($\langle 100\rangle$), and third ($\frac{1}{2}\langle 211\rangle$) neighbors, and less than 10 meV for fourth neighbors ($\langle 110\rangle$) and beyond. We use the nomenclature of Ref. 18. For $\Delta E^{(1)}_{1..}$, $\Delta E^{(3)}_{1..}$, and $\Delta E^{(4)}_{1..}$, there are multiple barriers between different vacancy-Si configurations; in all cases, a vacancy makes a jump along nearest neighbor $\frac{1}{2}\langle 110\rangle$ directions (giving the initial 1 subscript), and the parentheses indicate the final and initial positions of the vacancy (e.g., a vacancy jump from first to second neighbor of Si is 21, with barrier $\Delta E^{(1)}_{121}$).

$\Delta E^{(0)}_{1}$	vacancy jump	1.074
$\Delta E^{(1)}_{1..}$	vacancy-solute rotation (11, 21, 12)	1.003, 1.213, 1.101
	vacancy-solute rotation (32, 23, 33)	1.091, 1.058, 1.089
	vacancy-solute rotation (31, 13)	1.153, 1.008
$\Delta E^{(2)}_{1}$	vacancy-solute exchange	0.891
$\Delta E^{(3)}_{1..}$	vacancy-solute dissociation (41, 42, 43)	1.128, 1.066, 1.068
$\Delta E^{(4)}_{1..}$	vacancy-solute association (14, 24, 34)	1.028, 1.077, 1.112

correction from the effective Hamiltonian, thus providing transport coefficients in terms of the atomic scale jumps. We developed a systematic numerical method that goes beyond the small number of distinct frequencies previously considered in analytic solutions, which allows us to account for anisotropic transport coefficients in systems under strain.[21]

II. METHODOLOGY

We use first-principles methods to compute energy barriers and their derivatives with strain for atomic jumps. The calculations are performed with VASP,[22,23] a plane-wave density-functional theory (DFT) code. Ni and Si are treated with ultrasoft Vanderbilt type pseudopotentials[24,25] using Ar and Ne cores, respectively, and the local density approximation[26] as parameterized by Perdew and Zunger.[27] We use a single vacancy in a 107-atom ($3 \times 3 \times 3$ along cube axes) nickel supercell with a substitutional silicon atom, and a $8 \times 8 \times 8$ k-point mesh. A 420 eV plane-wave cutoff is converged to 1 meV/atom, and the k-point mesh with Methfessel-Paxton smearing of 0.1 eV is converged to 1 meV/atom. To compute energy barriers, we use the climbing-image nudged elastic band[28,29] method with one intermediate image and constant cell shape to find transition pathways. Along the path, the force is negated, while components perpendicular to the path are unchanged; the image relaxes to an extremum with forces less than 5 meV/Å, and restoring forces confirm this extremum as a first-order saddle point. The attempt frequency prefactor for each transition is estimated with the Vineyard equation[30] in a hopping-atom approximation, the errors of which are estimated in the Appendix. The derivatives of energy barriers with respect to strain are computed with finite difference of ±0.01 strains.

III. RESULTS

A. Energy barriers

Table I gives the energy barriers for atomic jumps in FCC Ni. The "five-frequency" model[19,20] considers five atomic jumps, all involving a vacancy moving along nearest-neighbor directions $\frac{1}{2}\langle 110\rangle$: a vacancy in Ni jumping without Si, the vacancy neighboring a Si atom jumping to another neighboring site, a vacancy exchanging with a Si atom, and the dissociation and association of a vacancy and a Si atom. This assumes the solute and vacancy interact at the first neighbor only, while DFT shows an attractive–0.100 eV first neighbor interaction and a repulsive +0.045 eV third neighbor interaction. We include this interaction in the transport coefficient computation with additional jumps: 16 total jumps in the strain-free case. Note that, except for the solute jump $\Delta E^{(2)}$ and the vacancy jump $\Delta E^{(1)}$ between first neighbors, forward and reverse energy barriers average to ±0.015 eV of the vacancy jump $\Delta E^{(0)}$; this means beyond first neighbors, different barriers result mainly from the site energy changes. Except for the vacancy jump in Ni with a prefactor of 4.8 THz, we find prefactors of 5.0–5.3 THz (see the Appendix). Figure 1(a) shows the ratio $L_{\mathrm{SiV}}/L_{\mathrm{SiSi}}$ where a sign change occurs at a crossover temperature of $T_{\mathrm{cross}} = 1060$ K; below this temperature, Si diffusion is dominated by complexes ("solute drag").[31] The transition temperature is consistent with the strength of the Si-vacancy binding energy.

B. Strain derivatives

The derivative of macroscopic L_{AB} with respect to strain is the fourth-rank elastodiffusion tensor, with three independent entries for cubic symmetry.[13,32] Strain and transport coefficients are both symmetric second rank tensors, so the derivative $L'_{abcd} = dL_{ab}/d\varepsilon_{cd}|_{\varepsilon=0}$ is symmetric for ab and

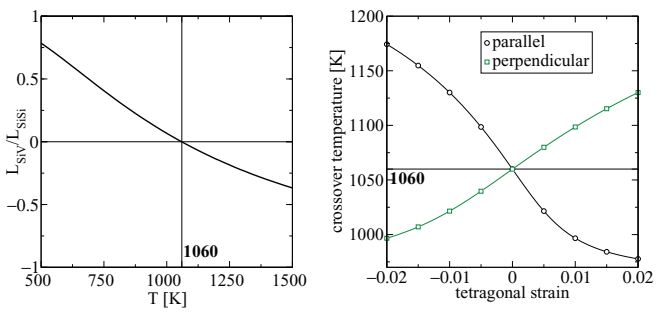

FIG. 1. (Color online) (a) Ratio of $L_{\mathrm{SiV}}/L_{\mathrm{SiSi}}$ for Si in Ni, showing the crossover from solute-drag below 1060 K to vacancy-exchange dominated diffusion above 1060 K, and (b) change in crossover temperature with tetragonal strain $e_3 = -2e_1 = -2e_2$ along parallel [001] and perpendicular $\langle 100\rangle$ directions.

cd, and benefits from using a contracted Voigt notation like the elastic constants C_{ij}.[13] Similarly, if the cubic axes are chosen as x, y, and z, then the derivatives $L'_{11} = L'_{22} = L'_{33}$, $L'_{12} = L'_{21} = L'_{13} = L'_{31} = L'_{23} = L'_{32}$, and $L'_{44} = L'_{55} = L'_{66}$ while all other components are zero. A further simplification is possible: We represent the elastodiffusion tensors with the volumetric derivative L^{v}, a tetragonal strain derivative L^{t}, and a [100](010) shear derivative L^{s}. The strain tensor $\underline{\varepsilon}$ has six independent components e_1 through e_6 and can be written

$$\frac{1}{3}\varepsilon_{\mathrm{v}}\underline{1} + \begin{pmatrix} e_1 - \frac{1}{3}\varepsilon_{\mathrm{v}} & 0 & 0 \\ 0 & e_2 - \frac{1}{3}\varepsilon_{\mathrm{v}} & 0 \\ 0 & 0 & e_3 - \frac{1}{3}\varepsilon_{\mathrm{v}} \end{pmatrix} + \begin{pmatrix} 0 & \frac{1}{2}e_6 & \frac{1}{2}e_5 \\ \frac{1}{2}e_6 & 0 & \frac{1}{2}e_4 \\ \frac{1}{2}e_5 & \frac{1}{2}e_4 & 0 \end{pmatrix}, \tag{3}$$

where $\varepsilon_{\mathrm{v}} = e_1 + e_2 + e_3$; let $\underline{\varepsilon}^{\mathrm{t}}$ and $\underline{\varepsilon}^{\mathrm{s}}$ be the final two tensors. Then the $\underline{L}(\underline{\varepsilon})$ tensor is

$$\underline{L} = L^0\underline{1} + L^{\mathrm{v}}\tfrac{1}{3}\varepsilon_{\mathrm{v}}\underline{1} + L^{\mathrm{t}}\underline{\varepsilon}^{\mathrm{t}} + L^{\mathrm{s}}\underline{\varepsilon}^{\mathrm{s}}, \tag{4}$$

where L^0 is the stress-free value, following Ref. 13.

The changes in microscopic jump barriers with hydrostatic strain are characterized by changes in local geometry without a change in symmetry, and so the number of transitions remains unchanged. Volumetric strain couples to vacancy energy ($\alpha_{\mathrm{V}} = 18.1$ eV) and Si solute energy ($\alpha_{\mathrm{Si}} = -2.05$ eV) but weakly with vacancy-binding energy (−0.37 eV energy derivative). For Si in Ni, we found all barriers modified by the same amount to first order in volumetric strain. The barriers change by −7 eV times the fractional length change ($\varepsilon_{\mathrm{v}}/3$) for volumetric strain ε_{v}; here, lattice expansion gives higher jump rates. Hence, the derivative $L^{\mathrm{v}} = L^0 \cdot (7\mathrm{eV}/k_{\mathrm{B}}T)$ for all L_{AB}; moreover, the crossover temperature is to first-order independent of lattice constant and insensitive to thermal expansion.

The two shears—tetragonal and [100](010) shear—produce changes in local geometry, and lowered symmetry increases the number of independent jumps. Tetragonal shear ($e_3 = -2e_1 = -2e_2$, all others zero) breaks cubic symmetry, and the twelve ⟨110⟩ vectors break into two groups: four ⟨110⟩ and eight ⟨011⟩ vectors with fractional length changes of $-e_3/2$ and $e_3/4$, respectively.[1] The jumps are fully characterized by the vector between the Si atom and vacancy position before and after the jump. In the five frequency model, the lifted degeneracy results in two different $\Delta E^{(0)}$ and $\Delta E^{(2)}$ jumps, and 3 $\Delta E^{(1)}$, and 4 $\Delta E^{(3)}$, and $\Delta E^{(4)}$ types of jumps for a total of 15 jump frequencies. Accounting for third-neighbor Si-V interactions, the 16 stress-free frequencies become $2 + 22 + 2 + 9 + 9 = 44$. For Si in Ni, first-principles calculations show that the energy barrier change is mostly determined by the particular jump vector direction alone, where the barrier change is 15.5 eV times the fractional length change ($-e_3/2$ or $e_3/4$). The difference compared with volumetric strain is a consequence of the transition state geometry: Tetragonal strain *expands* the lattice at the transition state when *decreasing* the distance for the jump, in contrast to volumetric strain. In addition, there is little change in the Si-vacancy binding energy with tetragonal strain. For an [100](010) shear ($e_6 \neq 0$, all others zero), the number of independent jumps increases even further; however, the energy barrier changes with respect to strain are nearly an order of magnitude smaller than volumetric or tetragonal shears—a maximum change of 1.2 eV times the shear strain—and hence are ignored in this study.

Figure 1(b) shows the change in crossover temperature due to tetragonal strain along perpendicular directions, and Table II summarizes values and derivatives for transport coefficients near the crossover temperature. With a tetragonal strain ($e_3 = -2e_1 = -2e_2$, $\varepsilon_{\mathrm{v}} = 0$), Eq. (4) gives opposite signs along parallel and perpendicular directions. In particular, at the crossover temperature T_{cross} where $L^0_{\mathrm{SiV}} = 0$, $L_{\mathrm{SiV},33}$ has a sign opposite to $L_{\mathrm{SiV},11}$ and $L_{\mathrm{SiV},22}$—that is, solute drag happens in one ⟨100⟩ direction, but solute exchange in perpendicular directions. Thus, *different crossover temperatures* are found in parallel and perpendicular directions for a fixed tetragonal strain. In the small strain limit, symmetry imposes the ratio of derivatives of T_{cross} with strain in the parallel direction to perpendicular direction to be -2 [c.f. Eq. (4)]; at larger strains, T_{cross} is nonlinear due to different temperature dependence of L^0_{SiV} and $L^{\mathrm{t}}_{\mathrm{SiV}}$. Note that the changes from tetragonal strain are entirely caused by changes in jump barriers without any significant changes in Si-vacancy binding energy.

C. Initial flow near a dislocation

One consequence of the anisotropy in transport coefficients due to strain is the creation of complex solute flow in the

TABLE II. Transport coefficients [mol/(eV Å ns)] and derivatives below, at, and above the crossover temperature. In the dilute limit, L_{VV} is proportional to c_{V} while L_{SiV} and L_{SiSi} are proportional to $c_{\mathrm{V}}c_{\mathrm{Si}}$.

		L^0	L^{v}	L^{t}
960 K	VV	$1.52 \times 10^{-1} c_{\mathrm{V}}$	$1.29 \times 10^{1} c_{\mathrm{V}}$	$-7.42 \times 10^{0} c_{\mathrm{V}}$
	SiV	$1.57 \times 10^{-1} c_{\mathrm{V}}c_{\mathrm{Si}}$	$1.33 \times 10^{1} c_{\mathrm{V}}c_{\mathrm{Si}}$	$-2.24 \times 10^{1} c_{\mathrm{V}}c_{\mathrm{Si}}$
	SiSi	$1.29 \times 10^{0} c_{\mathrm{V}}c_{\mathrm{Si}}$	$1.09 \times 10^{2} c_{\mathrm{V}}c_{\mathrm{Si}}$	$-5.08 \times 10^{1} c_{\mathrm{V}}c_{\mathrm{Si}}$
1060 K	VV	$4.69 \times 10^{-1} c_{\mathrm{V}}$	$3.59 \times 10^{1} c_{\mathrm{V}}$	$-2.08 \times 10^{1} c_{\mathrm{V}}$
	SiV	0	0	$-3.72 \times 10^{1} c_{\mathrm{V}}c_{\mathrm{Si}}$
	SiSi	$3.27 \times 10^{0} c_{\mathrm{V}}c_{\mathrm{Si}}$	$2.51 \times 10^{2} c_{\mathrm{V}}c_{\mathrm{Si}}$	$-1.16 \times 10^{2} c_{\mathrm{V}}c_{\mathrm{Si}}$
1160K	VV	$1.18 \times 10^{0} c_{\mathrm{V}}$	$8.27 \times 10^{1} c_{\mathrm{V}}$	$-4.80 \times 10^{1} c_{\mathrm{V}}$
	SiV	$-7.55 \times 10^{-1} c_{\mathrm{V}}c_{\mathrm{Si}}$	$-5.29 \times 10^{1} c_{\mathrm{V}}c_{\mathrm{Si}}$	$-4.65 \times 10^{1} c_{\mathrm{V}}c_{\mathrm{Si}}$
	SiSi	$7.02 \times 10^{0} c_{\mathrm{V}}c_{\mathrm{Si}}$	$4.92 \times 10^{2} c_{\mathrm{V}}c_{\mathrm{Si}}$	$-2.25 \times 10^{2} c_{\mathrm{V}}c_{\mathrm{Si}}$

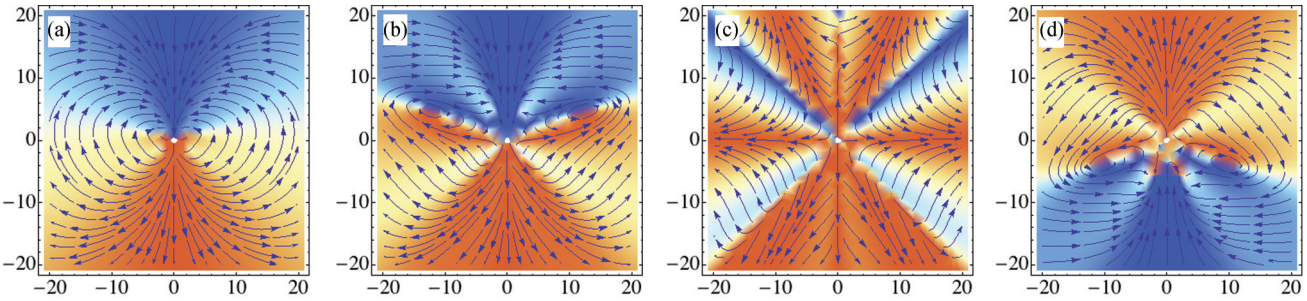

FIG. 2. (Color online) Initial flow streams from Eq. (1) around a dislocation for (a) vacancies, (b) Si 50 K below the effective crossover, (c) Si at the effective crossover, and (d) Si 50 K above the effective crossover temperature. The initial Si and vacancy distribution is homogeneous, allowing fluxes to be found analytically throughout all space. The spatial dimensions are in units of the Burgers vector (2.49 Å) for an edge dislocation in Ni placed at the origin, with the $[1\bar{1}0]$ horizontal and [111] vertical, in the $(11\bar{2})$ plane. The coloring shows the cosine of the flow direction with the radial vector $\hat{r}$, where orange is flow away from the dislocation core, blue is flow to the core, and white is orthogonal to $\hat{r}$.

presence of heterogeneous strain fields. To illustrate this phenomenon, we consider a dislocation. A natural coordinate system for an edge dislocation is the Burgers vector $\vec{b} = \frac{a}{2}[1\bar{1}0]$, slip plane normal $\vec{n} = [111]$, and threading vector $\vec{t} = [11\bar{2}]$. To highlight the anisotropy of transport coefficients, for simplicity we use isotropic elasticity: The three strain components that couple to transport coefficients when $L^{\mathrm{s}} \approx 0$ are volumetric strain $\varepsilon_{\mathrm{v}} = -b\sin\theta/4\pi r$, shear strain $\varepsilon_{bn} = 3b(\cos\theta + \cos 3\theta)/16\pi r$, and Burgers-vector normal strain $\varepsilon_{bb} = -b(4 + 3\cos 2\theta)\sin\theta/8\pi r$, where r is the distance from the dislocation, and θ is the angle from the slip plane. These strain fields produce anisotropic transport coefficients, and provide a driving force for both solutes and vacancies due to the change in chemical potential from volumetric strain in Eq. (2). The L_{AB} in dislocation coordinate system for an edge dislocation in FCC has a particular spatially-dependent transport coefficient tensor, with varying amount of anisotropy. In the $\vec{b} \times \vec{n}$ plane, the anisotropic transport tensor is

$$\begin{pmatrix} L^0 + \frac{1}{3}L^{\mathrm{v}}\varepsilon_{\mathrm{v}} + \frac{1}{6}L^{\mathrm{t}}\varepsilon_{bb} & \frac{2}{3}L^{\mathrm{t}}\varepsilon_{bn} \\ \frac{2}{3}L^{\mathrm{t}}\varepsilon_{bn} & L^0 + \frac{1}{3}L^{\mathrm{v}}\varepsilon_{\mathrm{v}} \end{pmatrix} \tag{5}$$

Here, we restrict to initially uniform vacancy and solute fields; this creates a Si flux given by $-(\underline{L}_{\mathrm{SiV}}\alpha_{\mathrm{V}} + \underline{L}_{\mathrm{SiSi}}\alpha_{\mathrm{Si}})\nabla\varepsilon_{\mathrm{v}}$ where $\nabla\varepsilon_{\mathrm{v}} = (-\hat{r}\sin\theta + \hat{\theta}\cos\theta)b/4\pi r^2$. The unstrained combination $L^0_{\mathrm{SiV}}\alpha_{\mathrm{V}} + L^0_{\mathrm{SiSi}}\alpha_{\mathrm{Si}}$ changes sign at approximately 970 K (c.f., Table II)—this is an effective crossover temperature $T^{\mathrm{eff}}_{\mathrm{cross}}$ for solute-drag from a strain-gradient driving force. Note that anisotropy in the transport tensor is entirely due to L^{t} and coupling with ε_{bn} and ε_{bb} strain components.

Figure 2 shows initial flow patterns for vacancies and Si from a dislocation strain field. For the vacancy, the L^0 and L^{v} components dominate over L^{t} at most temperatures, and so the initial flow is closely proportional to $\nabla\varepsilon_{\mathrm{v}}$; vacancies flow from tensile stressed region below the slip plane to compressive stressed region above the slip plane. However, for Si, anisotropy in Eq. (5) produces very unusual flow patterns. At the effective crossover temperature $T^{\mathrm{eff}}_{\mathrm{cross}}$ in Fig. 2(c), the dominant contribution to L_{SiV} are from $L^{\mathrm{t}}_{\mathrm{SiV}}$, leading to Si flux out of the dislocation core *in all directions* despite vacancy transport circuits around the dislocation. Moreover, solute flows *perpendicular* to vacancy flow near the slip plane. Below the effective crossover temperature, solute drag is prevalent so that Si flow mostly follows vacancy flux; however, even 50 K below $T^{\mathrm{eff}}_{\mathrm{cross}}$, anisotropy of L_{SiV} leads to diffusional circuits on opposite sides of the dislocation as ε_{bb} and ε_{nb} change magnitudes. Similarly, above the effective crossover temperature, solute exchange is prevalent so that Si flow is mostly opposite to vacancy flux, and anisotropy produces circuits. The size of the region of strong anisotropy around the dislocation scales as $1/|T - T^{\mathrm{eff}}_{\mathrm{cross}}|$. As point defects evolve in time, the distribution of Si will change, which will modify the chemical potentials and vacancy flux; we expect anisotropy to affect Si segregation patterns near a dislocation core, and creep rates. As the method can be adapted to include interstitial transport,[33] the study of irradiation-induced precipitation is possible.[34]

IV. CONCLUSIONS

We expect such complex flow of solute near a dislocation, or other defects, to occur in other systems. The change in crossover temperatures due to tetragonal strain is a consequence of fundamental symmetry, and hence, completely general. The primary requirement is an effective crossover temperature $T^{\mathrm{eff}}_{\mathrm{cross}}$ in a range where solute diffusion is non-negligible. This is the situation for FCC and BCC alloys, such as Ni-Cr,[35] Al-Si and Al-Cu,[15] and Fe-Cu.[36] Other systems could exhibit more complex flow patterns if, for example, volumetric strain changed the crossover temperature, or if L^{s} were comparable to L^{v} and L^{t}. The change of transport coefficients with strain impacts many important phenomena. In addition to segregation and creep, the rate of precipitation and topology of precipitates formed near a dislocation will be affected. Other sources of heterogeneous strain fields in a material—such as grain boundaries, secondary phases, voids, bubbles—can attract vacancies and solutes. Beyond the illustration of complex solute flow, the computation of transport coefficients and their strain derivatives from first principles combined with SCMF enables multiscale modeling for diffusion-controlled evolutions of microstructures.

ACKNOWLEDGMENTS

The authors thank R. S. Averback for helpful conversations. Research supported by the US Department of

Energy, Office of Basic Energy Sciences, Division of Materials Sciences and Engineering under Award No. DE-FG02-05ER46217, through the Frederick Seitz Materials Research Laboratory with computing resources from NERSC and the Taub cluster at the University of Illinois at Urbana-Champaign.

APPENDIX: PREFACTOR COMPUTATION

To compute the attempt frequency using the Vineyard equation from harmonic transition state theory[30] for each transition, we use the restoring forces on the jumping atom only. This approximation leaves out the coupling of the jumping atom vibration to the vibration of the other atoms. To estimate the error induced by ignoring this term, we first computed the attempt frequency for the five frequencies of the five frequency model in a $2 \times 2 \times 2$ supercell and considered an increasing number of modes. That is, if $\omega_1 > \omega_2 > \cdots > \omega_{3N}$ are the (ordered) normal modes from the starting configuration (for an N atom supercell) and $\omega'_1 > \omega'_2 > \cdots \omega'_{3N-1}$ are the (ordered) normal modes for the transition state, we compute

$$\frac{\prod_{i=1}^{n} \omega_i}{\prod_{i=1}^{n-1} \omega'_i} \tag{A1}$$

for increasing values of n, up to $3N = 93$. In general, lower frequencies correspond to less localized modes. Figure 3 shows the prefactors of the five atomic jumps as a function of the number of modes considered. It can be seen that all the frequencies have a similar behavior, decreasing with the number of modes and reaching a plateau when approximately 40 modes are taken into account. When more distant modes are taken into account, the plateau is near 60 modes and the value of each prefactor increases in an exponential manner. This last growth can be attributed to the accumulation of numerical error as the prefactor is a product of the frequencies of the modes considered. For the calculation of kinetic correlations, only the relative value of the prefactor is significant. Figure 3 shows the evolution of the prefactors of the different frequencies with the number of modes considered. The values are normalized by the prefactor $\nu^{(0)}$ of the jump frequency of the vacancy in bulk nickel. When up to 60 modes are considered, the different frequencies stay between 2/3 and 3/2 of the values of the vacancy jump in the bulk. The restriction to the forces on the jumping atom thus seems to be a meaningful approximation of the value of the different prefactor for the current problem.

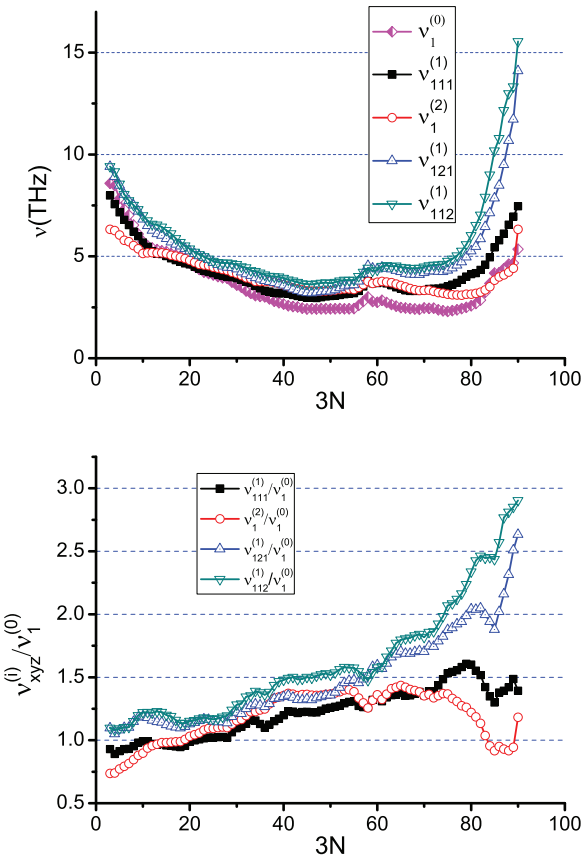

FIG. 3. (Color online) Values of the prefactors associated with five frequencies in THz (top) and relative to $\nu^{(0)}$ (bottom). The jumps are for a solute atom $\nu^{(2)}$, of the vacancy in the bulk $\nu^{(0)}$, of a rotation from a first to another first nearest neighbor site $\nu_{111}^{(1)}$, to a second nearest neighbor site $\nu_{121}^{(1)}$ and from a second to a first nearest neighbor site $\nu_{112}^{(1)}$. The modes considered are ordered by decreasing frequencies; lower frequencies correspond to less localized vibrational modes.

To estimate the effect of the inaccuracy of the prefactors on the transport properties, we determine the sensitivity of the crossover temperature T_{cross} to the value of the prefactors. In the unstrained case, the drag ratio $L_{\text{SiV}}/L_{\text{SiSi}}$ is a nonlinear function of 16 frequencies. If the binding entropy is assumed to be accurate, the sensitivity with respect to nine different independent prefactor must be studied. Figure 4 shows calculations of this ratio for the 512 sets of values of the prefactors that corresponds to all possible cases where each of these independent parameter takes either the value $3/2\nu^{(0)}$ or $2/3\nu^{(0)}$. This figure shows the most extreme variations that can be expected from the variations of the prefactors induced by the approximation performed in their calculation. The frequency associated with a displacement of the vacancy from a nearest

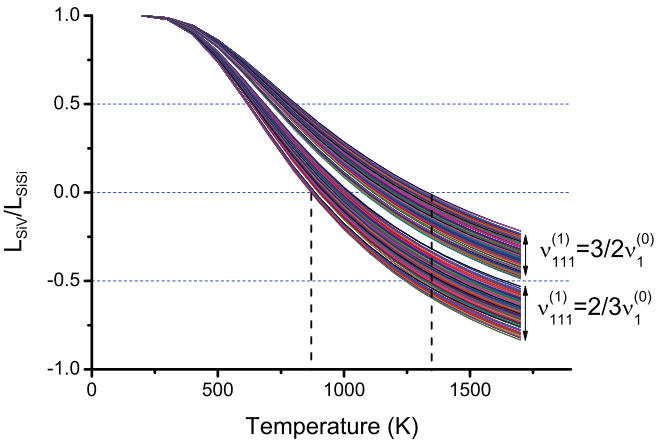

FIG. 4. (Color online) Ratio of $L_{\text{SiV}}/L_{\text{SiSi}}$ for dilute Si in Ni as a function of the temperature. For each curve, the value of each of the prefactors takes either the value $3/2\nu^{(0)}$ or $2/3\nu^{(0)}$.

neighbor site of the solute towards another nearest neighbor site has the most influence: In all cases a crossover takes place, and the crossover temperature T_{cross} remains between 800 and 1400 K. The density functional theory results can predict the value of the crossover temperature to within a few hundred degrees. However, the crossover temperature remains below the melting point of the alloy and in a temperature region with significant mobility for vacancies and Si. Hence, the qualitative behavior of the Ni-Si dilute alloy is robust with respect to variations of the prefactors, and the unusual flow patterns—which rely on the broken macroscale symmetry—are robust.

*dtrinkle@illinois.edu

[1] A. Ardell and S. Prikhodko, Acta mater. **51**, 5013 (2003).
[2] M. J. Aziz, Appl. Phys. Lett. **70**, 2810 (1997).
[3] M. S. Daw, W. Windl, N. N. Carlson, M. Laudon, and M. P. Masquelier, Phys. Rev. B **64**, 045205 (2001).
[4] M. J. Aziz, Y. Zhao, H.-J. Gossmann, S. Mitha, S. P. Smith, and D. Schiferl, Phys. Rev. B **73**, 054101 (2006).
[5] R. G. A. Veiga, M. Perez, C. S. Becquart, C. Domain, and S. Garruchet, Phys. Rev. B **82**, 054103 (2010).
[6] R. G. A. Veiga, M. Perez, C. Becquart, E. Clouet, and C. Domain, Acta Mater. **59**, 6963 (2011).
[7] E. J. Savino, Philos. Mag. **36**, 323 (1977).
[8] C. H. Woo and C. B. So, Philos. Mag. A **80**, 1299 (2000).
[9] H. Ceric, R. Lacerda de Orio, J. Cervenka, and S. Selberherr, AIP Conf. Proc. **1143**, 56 (2009).
[10] D. J. Shu, F. Liu, and X. G. Gong, Phys. Rev. B **64**, 245410 (2001).
[11] F. C. Larche and J. W. Cahn, Acta metall. **30**, 1835 (1982).
[12] W. L. Chan, R. S. Averback, and Y. Ashkenazy, J. Appl. Phys. **104**, 023502 (2008).
[13] P. H. Dederichs and K. Schroeder, Phys. Rev. B **17**, 2524 (1978).
[14] A. Janotti, M. Krčmar, C. L. Fu, and R. C. Reed, Phys. Rev. Lett. **92**, 085901 (2004).
[15] M. Mantina, Y. Wang, L. Q. Chen, Z. K. Liu, and C. Wolverton, Acta Mater. **57**, 4102 (2009).
[16] M. Nastar, V. Y. Dobretsov, and G. Martin, Philos. Mag. A **80**, 155 (2000).
[17] M. Nastar, Philos. Mag. **85**, 3767 (2005).
[18] T. Garnier, M. Nastar, P. Bellon, and D. R. Trinkle, Phys. Rev. B **88**, 134201 (2013).
[19] A. B. Lidiard, Philos. Mag. **46**, 1218 (1955) (http://www.tandfonline.com/doi/abs/10.1080/14786441108520633).
[20] A. D. Leclaire and A. B. Lidiard, Philos. Mag. **1**, 518 (1956).
[21] T. Garnier, P. Bellon, D. R. Trinkle, and M. Nastar (unpublished).
[22] G. Kresse and J. Hafner, Phys. Rev. B **47**, RC558 (1993).
[23] G. Kresse and J. Furthmüller, Phys. Rev. B **54**, 11169 (1996).
[24] D. Vanderbilt, Phys. Rev. B **41**, 7892 (1990).
[25] G. Kresse and J. Hafner, J. Phys.: Condens. Matter **6**, 8245 (1994).
[26] D. M. Ceperley and B. J. Alder, Phys. Rev. Lett. **45**, 566 (1980).
[27] J. P. Perdew and A. Zunger, Phys. Rev. B **23**, 5048 (1981).
[28] H. Jónsson, G. Mills, and K. W. Jacobsen, in *Classical and Quantum Dynamics in Condensed Phase Simulations*, edited by B. J. Berne, G. Ciccotti, and D. F. Coker (World Scientific, Singapore, 1998), p. 385.
[29] G. Henkelman, B. P. Uberuaga, and H. Jónsson, J. Chem. Phys. **113**, 9901 (2000).
[30] G. H. Vineyard, J. Phys. Chem. Solids **3**, 121 (1957).
[31] A. R. Allnatt and A. B. Lidiard, *Atomic transport in solids* (Cambridge University Press, Cambridge, 1993), Chap. 5, pp. 202–203.
[32] C. P. Flynn, *Point defects and diffusion* (Clarendon Press, Oxford, 1972) .
[33] V. Barbe and M. Nastar, Phys. Rev. B **76**, 054206 (2007).
[34] A. Barbu and A. J. Ardell, Scr. Metall. **9**, 1233 (1975).
[35] J. D. Tucker, R. Najafabadi, T. R. Allen, and D. Morgan, J. Nucl. Mater. **405**, 216 (2010).
[36] F. Soisson and C. C. Fu, Solid State Phenomena **139**, 107 (2008).